Supplementary Information

Coherent control of thermal phonon transport in van der Waals superlattices

Ruiqiang Guo[1], Young-Dahl Jho[2] and Austin J. Minnich[1,*]

[1] Division of Engineering and Applied Science, California Institute of Technology, Pasadena, California 91125, USA

[2] School of Electrical Engineering and Computer Science, Gwangju Institute of Science and Technology, Gwangju 61005, South Korea

[*] Corresponding author, aminnich@caltech.edu.

Supplementary Notes

Supplementary Note 1. Effect of strains on the κ_L of the $MoSe_2/WS_2$ superlattice

For the $MoSe_2/WS_2$ superlattice, confining the two materials to one unit cell leads to 2% tensile and compressive in-plane strains in the WS_2 and $MoSe_2$ layers compared to their bulk counterparts, respectively. To evaluate the influence of the strains on thermal transport, we first optimize the lattice parameters of bulk WS_2 and $MoSe_2$ by applying the corresponding strains and allowing the cross-plane lattice constants to relax. The obtained cross-plane lattice constants of WS_2 and $MoSe_2$ are decreased and increased by 1%, respectively. As a result, the cross-plane lattice constant of the $MoSe_2/WS_2$ superlattice is only 0.2% smaller than the average value of corresponding bulk crystals, a minor change compared to the in-plane ones.

We then calculate the κ_L of the two strained crystals, as shown in Figure S1. Compared to unstrained crystals, the in-plane thermal conductivity κ_{In} of the strained WS_2 at 300 K decreases from 153.5 to 129.3 W $m^{-1}K^{-1}$ while the cross-plane one κ_{Cross} increases from 3.9 to 4.2 W $m^{-1}K^{-1}$. For the $MoSe_2$, the 2% compressive strain increases the κ_{In} and κ_{Cross} at 300 K from 40.9 and 2.6 to 48.5 and 3.2 W $m^{-1}K^{-1}$, respectively. We now use the average value of κ_L in both bulk crystals to estimate that the κ_{In} of the $MoSe_2/WS_2$ superlattice decreases by 9% due to the 2% in-plane strains. For the κ_{Cross} of the superlattice, its variation is negligible considering the very small cross-plane strain. Therefore, the thermal anisotropy ratio $\kappa_{In}/\kappa_{Cross}$ of the strained superlattice may decrease by ~ 9%. These minor deviations caused by the strain effect thus will not affect our discussion and conclusion.

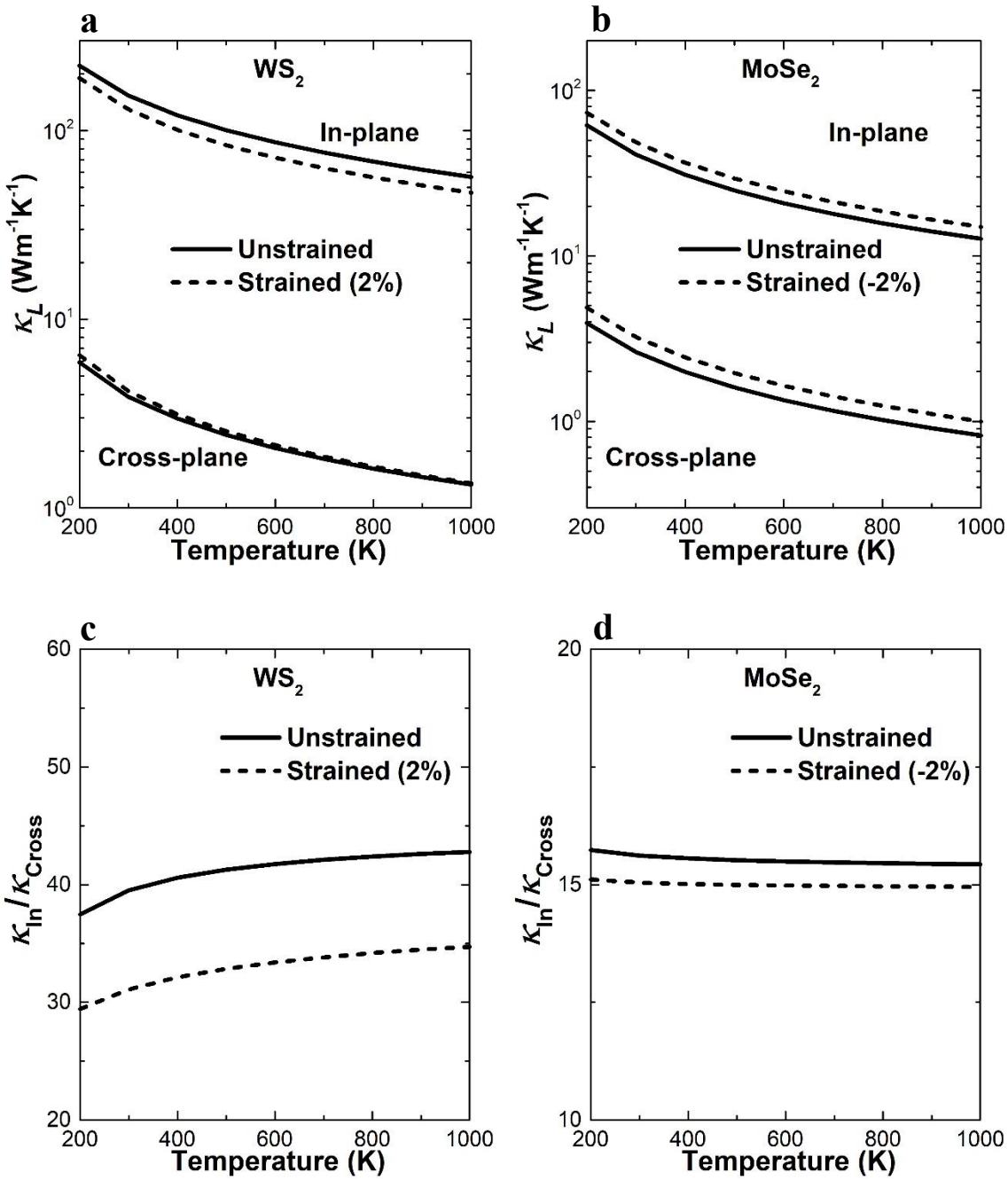

Figure S1. Effect of strains on thermal properties of bulk WS_2 and $MoSe_2$. (a, b) In-plane (top) and cross-plane (bottom) thermal conductivity κ_L and (c, d) thermal anisotropy $\kappa_{In}/\kappa_{Cross}$ versus temperature for bulk WS_2 and $MoSe_2$, respectively.

Supplementary Note 2. Effect of the impurity scattering on the κ_L in TMDCs

The calculated κ_L are generally relatively higher or close to the corresponding maximum experimental data. In principle, the well-established *ab initio* BTE approach predicts the upper limit of κ_L, representing that of perfect crystals. Prior *ab initio* calculations have reproduced experimental measurements for many materials[1-7], many of which were isotropic and for which high-quality samples were available. Experimental results may vary substantially due to sample impurities, geometries and measurement techniques. For anisotropic materials, the determination of the in- and cross-plane thermal conductivity on the same sample can be challenging.

Impurities may have a significant impact on the measured thermal conductivity values. Although the purity of currently synthesized samples can be larger than 99%, impurity scattering may still significantly suppress phonon transport, particularly for materials with high thermal conductivities. As a typical example, 0.1% boron impurities in WS_2 can decrease the κ_{In} and κ_{Cross} to 114.6 and 3.3 W $m^{-1}K^{-1}$ at 300 K, a reduction of 25.3% and 15.4% respectively. The impurity scattering more strongly suppresses the κ_{In} due to the significant contribution of higher frequency modes along this crystal plane, possibly explaining why our results agree better with the κ_{Cross} reported by Jiang et al[8]. The κ_{In} and κ_{Cross} are mainly contributed by phonons spanning a broader (0-7 THz) and narrower (0-2 THz) frequency range, respectively.

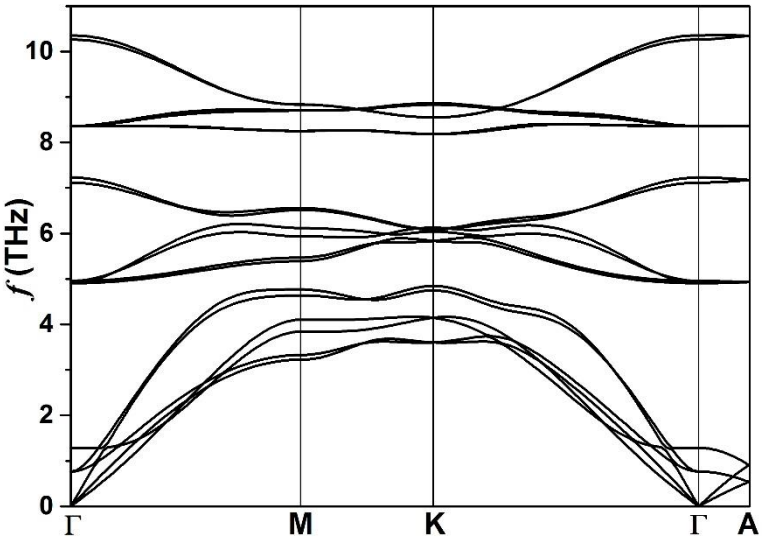

Figure S2. Phonon dispersion of bulk $MoSe_2$.

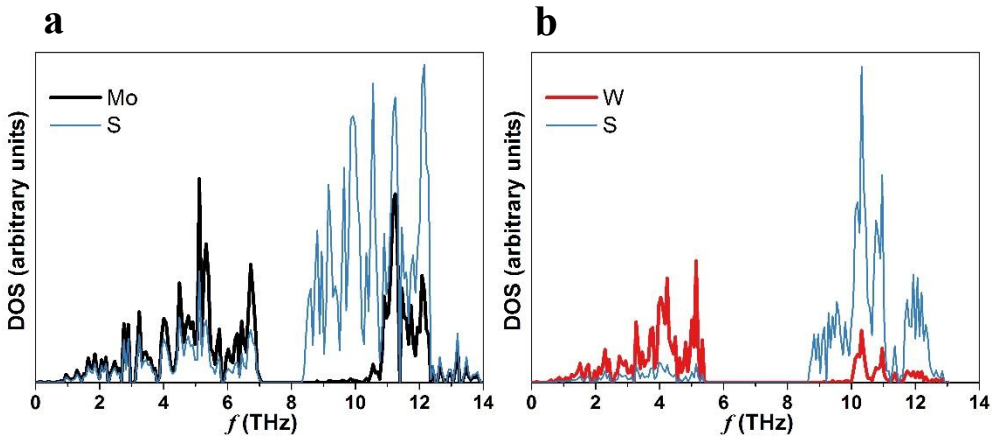

Figure S3. Partial phonon density of states of the bulk (a) MoS_2 and (b) WS_2. Heavier atoms (Mo, W) dominate the lattice vibrations at low frequencies while lighter ones (S) dominate those at high frequencies.

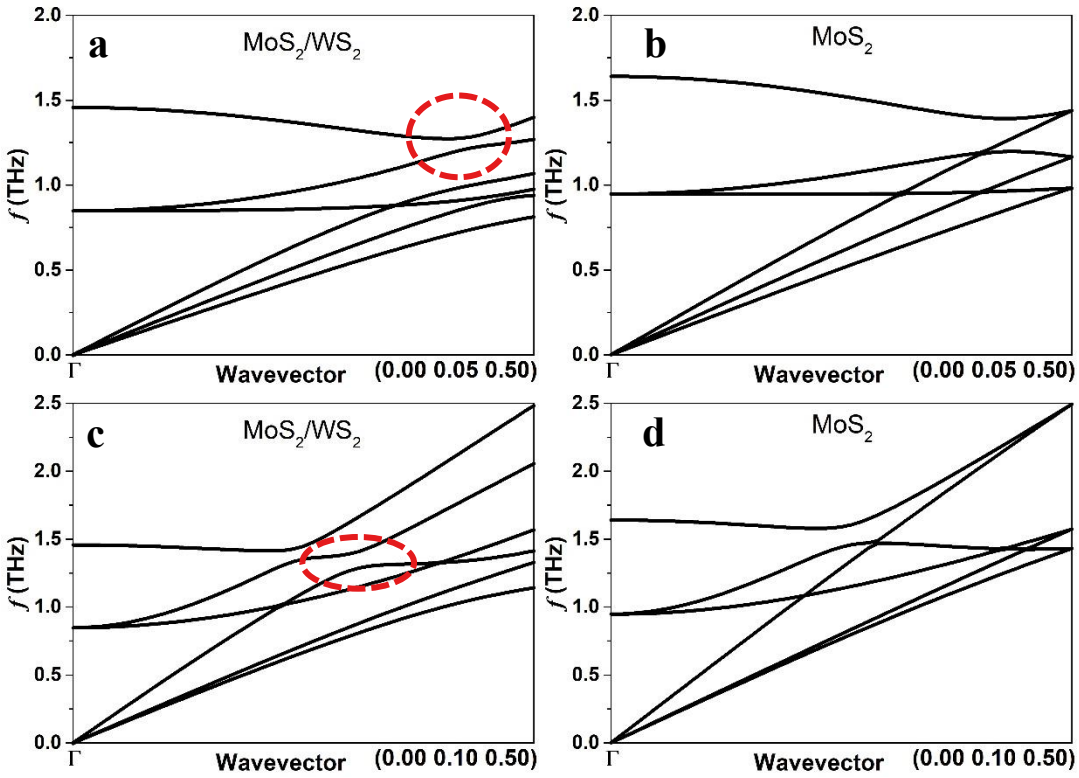

Figure S4. Anticrossing effects in superlattices. Phonon dispersions of the (a, c) MoS_2/WS_2 and (b, d) MoS_2 along two different Brillouin paths. The clear anticrossing effects (marked by red dashed lines) for the MoS_2/WS_2 superlattice substantially reduce group velocities.

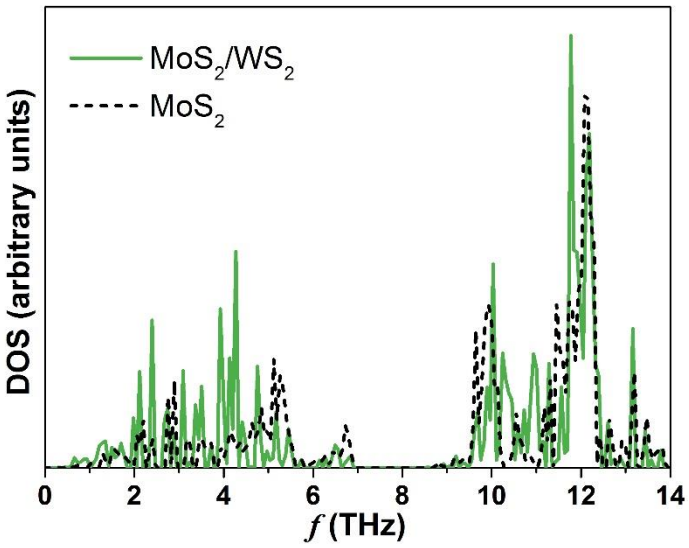

Figure S5. Phonon density of states projected along the *z* axis for the MoS_2/WS_2 superlattice and bulk MoS_2. Several sharp peaks for $f < 6$ THz in the density of states of the MoS_2/WS_2 superlattice result from the occurrence of band gaps at zone edges and anticrossings inside the zone.

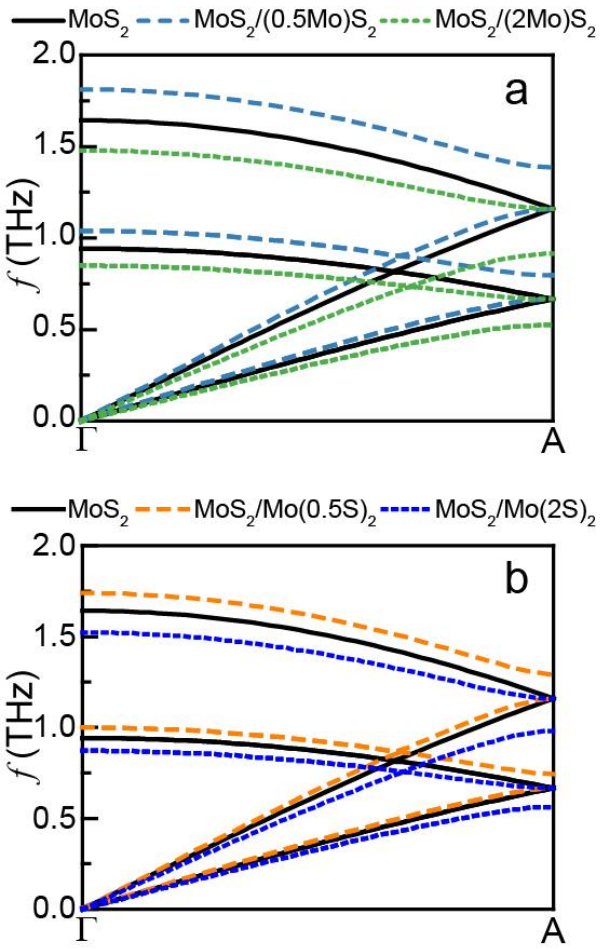

Figure S6. Effects of mass ratio on phonon dispersions. Phonon dispersions along the ΓA direction for (a) MoS_2, MoS_2/(0.5Mo)S_2 (half the atomic mass of Mo is used) and MoS_2/(2Mo)S_2 (twice the atomic mass of Mo), and (b) MoS_2, MoS_2/Mo(0.5S)$_2$ (half the atomic mass of S) and MoS_2/Mo(2S)$_2$ (twice the atomic mass of S). Increasing the mass difference leads to larger band gaps.

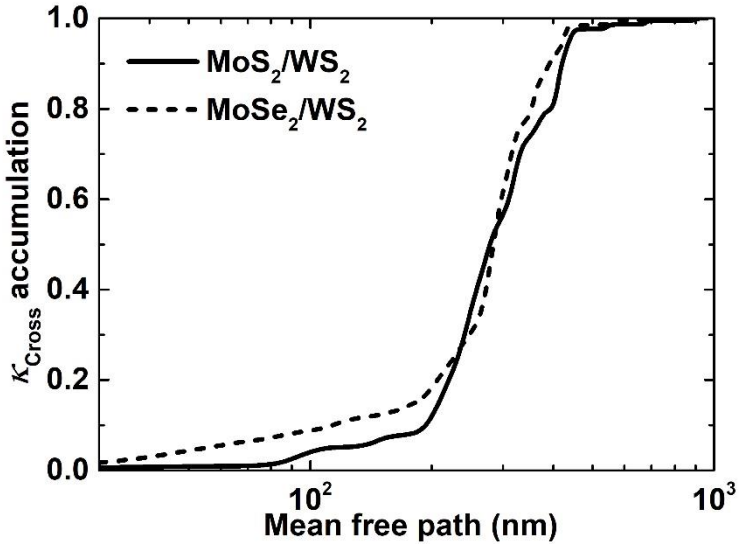

Figure S7. κ_{Cross} accumulation as a function of phonon mean free path for the MoS_2/WS_2 and $MoSe_2/WS_2$ superlattices. Most heat is carried by phonons with coherence lengths far exceeding the periodicity of around 1.2 nm for the superlattices.

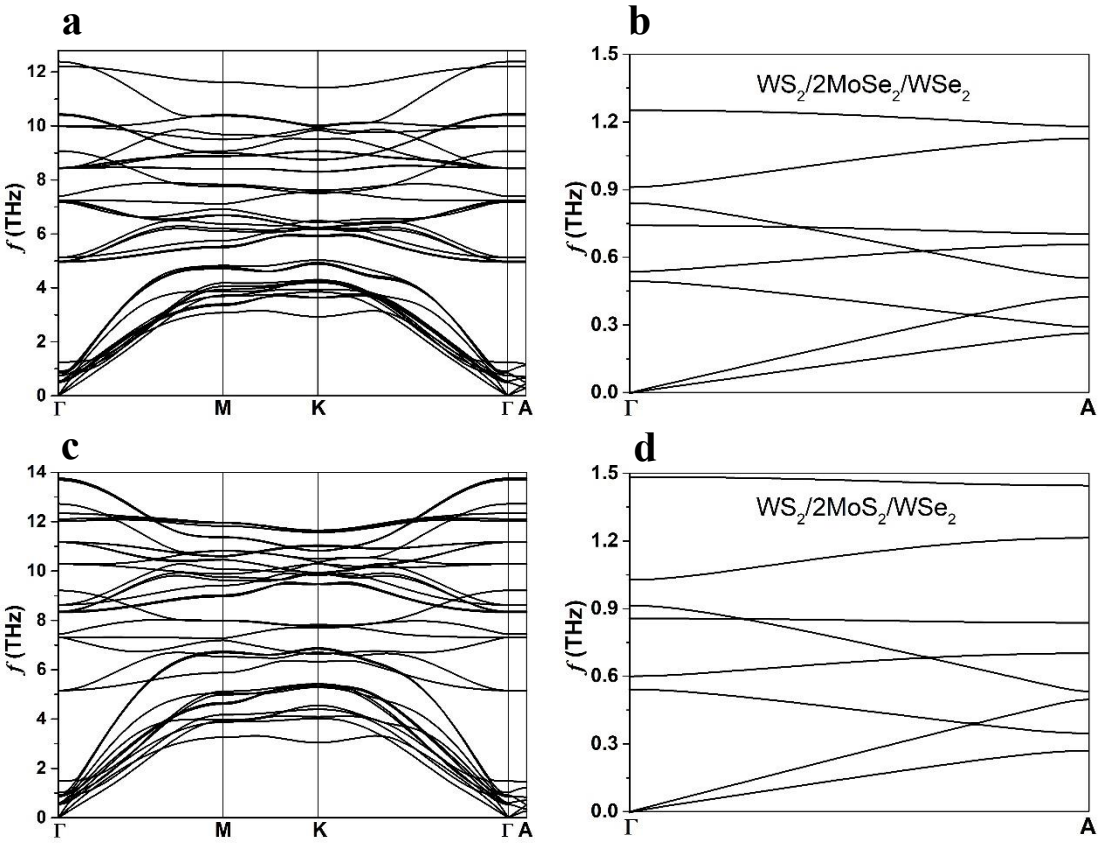

Figure S8. Phonon dispersions of the (a, b) $WS_2/2MoSe_2/WSe_2$ and (c, d) $WS_2/2MoS_2/WSe_2$ heterostructures. Zoom-ins of the twelve low-lying phonon branches along the ΓA direction are shown in (b) and (d). More significant band splitting along the in-plane directions and larger band gaps at zone edges are observed for the phonon dispersion of the $WS_2/2MoS_2/WSe_2$ heterostructure.

Supplementary References

1. Ward, A., Broido, D., Stewart, D. A. & Deinzer, G. Ab initio theory of the lattice thermal conductivity in diamond. *Phys. Rev. B* **80**, 125203 (2009).

2. Esfarjani, K., Chen, G. & Stokes, H. T. Heat transport in silicon from first-principles calculations. *Phys. Rev. B*, 085204 (2011).

3. Tian, Z. *et al*. Phonon conduction in PbSe, PbTe, and $PbTe_{1-x}Se_x$ from first-principles calculations. *Phys. Rev. B* **85**, 184303 (2012).

4. Lindsay, L., Broido, D. & Reinecke, T. Thermal conductivity and large isotope effect in GaN from first principles. *Phys. Rev. Lett.* **109**, 095901 (2012).

5. Wang, X. & Huang, B. Computational Study of In-Plane Phonon Transport in Si Thin Films. *Sci. Rep.* **4**, 6399 (2014).

6. Li, W. & Mingo, N. Lattice dynamics and thermal conductivity of skutterudites $CoSb_3$ and $IrSb_3$ from first principles: Why $IrSb_3$ is a better thermal conductor than $CoSb_3$. *Phys. Rev. B* **90**, 094302 (2014).

7. Guo, R., Wang, X. & Huang, B. Thermal conductivity of skutterudite $CoSb_3$ from first principles: Substitution and nanoengineering effects. *Sci. Rep.* **5**, 7806 (2015).

8. Jiang, P., Qian, X., Gu, X. & Yang, R. Probing Anisotropic Thermal Conductivity of Transition Metal Dichalcogenides MX_2 (M= Mo, W and X= S, Se) using Time-Domain Thermoreflectance. *Adv. Mater.* **29** (2017).